Deep and persistent melt layer in the Archaean mantle

Denis Andrault, Giacomo Pesce, Geeth Manthilake, Julien Monteux, Nathalie Bolfan-Casanova, Julien Chantel, Davide Novella, Nicolas Guignot, Andrew King, Jean-Paul Itié, et al.

nature geoscience

ARTICLES

https://doi.org/10.1038/s41561-017-0053-9

Deep and persistent melt layer in the Archaean mantle

Denis Andrault[1*], Giacomo Pesce[1,4], Geeth Manthilake[1], Julien Monteux[1], Nathalie Bolfan-Casanova[1], Julien Chantel[1], Davide Novella[1], Nicolas Guignot[2], Andrew King[2], Jean-Paul Itié[2] and Louis Hennet[3]

The transition from the Archaean to the Proterozoic eon ended a period of great instability at the Earth's surface. The origin of this transition could be a change in the dynamic regime of the Earth's interior. Here we use laboratory experiments to investigate the solidus of samples representative of the Archaean upper mantle. Our two complementary in situ measurements of the melting curve reveal a solidus that is 200–250 K lower than previously reported at depths higher than about 100 km. Such a lower solidus temperature makes partial melting today easier than previously thought, particularly in the presence of volatiles (H_2O and CO_2). A lower solidus could also account for the early high production of melts such as komatiites. For an Archaean mantle that was 200–300 K hotter than today, significant melting is expected at depths from 100–150 km to more than 400 km. Thus, a persistent layer of melt may have existed in the Archaean upper mantle. This shell of molten material may have progressively disappeared because of secular cooling of the mantle. Crystallization would have increased the upper mantle viscosity and could have enhanced mechanical coupling between the lithosphere and the asthenosphere. Such a change might explain the transition from surface dynamics dominated by a stagnant lid on the early Earth to modern-like plate tectonics with deep slab subduction.

Melting is a first-order phase transformation that has drastic consequences for various geophysically observable material properties, such as seismic-wave velocities and electrical conductivity (EC). As geological materials are chemically complex, they generally melt partially over a wide range of temperatures between their solidus and liquidus. In the early stages of the Earth's formation, extensive melting occurred down to great mantle depths, with the formation of a magma ocean, through the combination of radiogenic heating, impact-induced heating during accretionary events and gravitational energy release during core–mantle separation[1]. Partial melting can still occur today in the mantle, but at limited degrees of partial melting (F) and in specific regions. It occurs close to the Earth's surface when hot mantle materials undergo decompression, as at mid-ocean ridges. Also, seismic, magnetotelluric and electrical anomalies suggest the presence of melts at mantle depths between 80 and 200 km (ref. [2]), just atop the 410 km mantle discontinuity[3] and above the core–mantle boundary[4]. In these regions, thermochemical heterogeneities alone cannot explain the magnitude of anomalies.

Careful experiments are needed to address properly the evolution of the mantle solidus with pressure. Ideally, one should determine the onset of melting in the presence of the right amount of volatiles, such as CO_2 and H_2O, which unfortunately remains uncertain[5] and could vary from one geological setting to another. Generally, the dry solidus is used as a reference to which is added the role of volatiles[6]. The dry-solidus profile currently accepted for the upper mantle is derived from a few studies performed on KLB-1 peridotite[7–9], garnet peridotite[10], Allende meteorite[11] and the CMAS (CaO, MgO, Al_2O_3 and SiO_2) composition[12]. All these studies report melting temperatures significantly higher than the present-day temperature profile[13] (Supplementary Fig. 1). All previous studies used the so-called 'quench method' based on the analyses of recovered samples. This method is not well adapted to detect the onset of melting, which can correspond to F values smaller than 1 wt% in natural samples[14].

In this study, we determined the mantle solidus temperature using two independent in situ techniques, EC and X-ray diffraction, at pressures and temperatures up to 28 GPa and 2,300 K, in a multi-anvil apparatus.

Determination of the mantle solidus

Using EC, we first observed dehydration of the cell assembly, followed by crystallization of the glass starting material at a temperature below 1,573 K (Supplementary Fig. 5a). A complete sample dehydration and crystallization is evidenced by a perfect reproducibility of the sample conductivity when performing various cycles of cooling and heating. Full crystallization in this temperature range is also evidenced by analyses of the microstructure of quenched samples. On further heating, we observed a sudden increase of the slope in the EC profile, above a threshold temperature of 1,815–1,865 K (Fig. 1, Supplementary Fig. 5b and Supplementary Table 2). This can be interpreted as that just above the solidus temperature, F is very low in the sample and the melt wets only some specific grain surfaces, and not others, because the surface energy depends on its crystallographic orientation. With increasing temperature, the melt interconnection between the two electrodes improves. The melt progressively becomes the dominant conductive phase, with an ionic conduction mechanism[15]. Previous studies on partial melting report precisely the same behaviour in the evolution of sample conductivity with temperature[16–18].

Using X-ray diffraction, we first monitored the sample crystallization at temperatures from 1,200 K to 1,600 K (Supplementary Fig. 6), until the diffraction pattern remained independent of time. At this point, the set of diffractions peaks corresponded well with the expected mineralogy (Supplementary Fig. 7). We observed

[1]Université Clermont Auvergne, CNRS, IRD, OPGC, Laboratorie Magmas et Volcans, Clermont-Ferrand, France. [2]Synchrotron SOLEIL, Gif-sur-Yvette, France. [3]Conditions Extrêmes et Matériaux: Haute Température et Irradiation, CNRS, Orléans, France. Present address: [4]School of Geosciences, The University of Edinburgh, Edinburgh, UK. *e-mail: denis.andrault@uca.fr

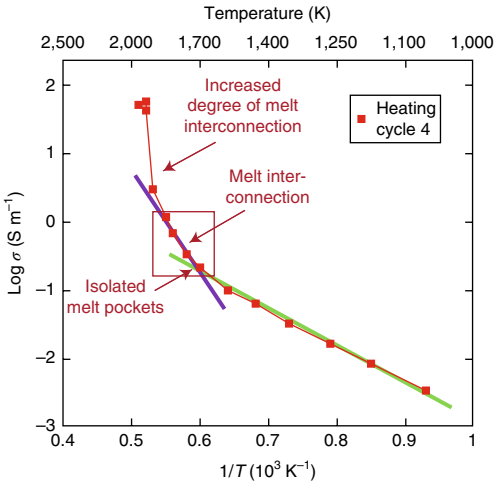

Fig. 1 | EC results. The sample EC was measured at increasing temperatures for a nominal pressure of 5 GPa after various pre-heating cycles. The clear change in slope at 1,700 K indicates a change in the conductivity mechanism at the onset of sample melting. A further increase of temperature induces a better interconnection of the melt between the electrodes, before ionic conduction in the interconnected melt becomes largely dominant (additional details are reported in Supplementary Fig. 5).

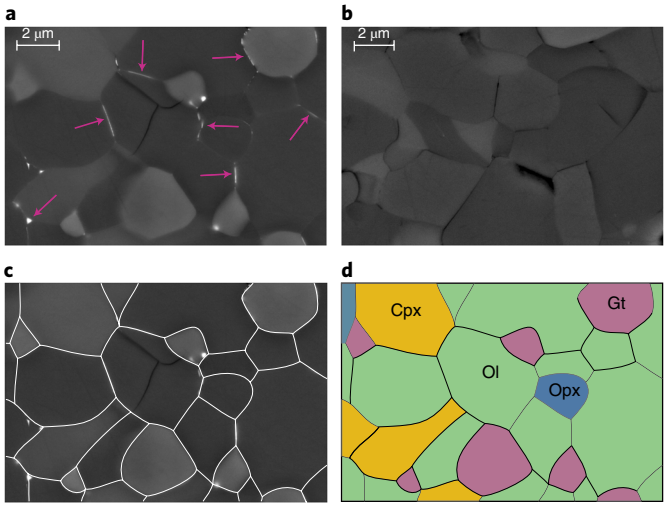

Fig. 2 | Images of recovered samples. a,**b**, Using the field-emission gun electron microscope, microphotographs were acquired on samples recovered after heating just above (**a**) and just below (**b**) the solidus temperature. In both cases, the pressure was 5 GPa. For a temperature above the solidus, very thin films and nanometre-size pockets of melt are clearly visible (pink arrows). **c**, The polygonal shape of grains is typical of good textural equilibrium. **d**, The sample mineralogy was refined from chemical map. Ol, olivine; Cpx, clinopyroxene; Gt, garnet; Opx, orthopyroxene.

olivine and its high-pressure polymorphs, and majoritic garnet and pyroxenes were also visible for pressures below ~14 GPa. At subsolidus conditions, the relative peak intensities were very compatible with those theoretically expected based on atomic topologies, which hence revealed an equilibrated microstructure. No significant changes were observed on further heating until the sample behaviour changed abruptly: all the diffraction peaks from the sample suddenly underwent major changes of their intensities with time. Large intensity variations could be seen in real time on diffraction profiles recorded by the Ge detector (Supplementary Fig. 8). Such instability denotes a fast grain rotation in the X-ray beam. We estimate that a grain rotation of less than 1° is enough to stop the diffraction signal of a grain previously oriented in ideal Bragg conditions. Decreasing the sample temperature by 10–20 K stopped entirely the rapid variation in peak intensities. Thus, this sudden change above a critical temperature is not compatible with a continuous increase with temperature of grain-growth rate. Instead, the observed fast grain rotation can be related to the presence of a thin film of melt at the grain boundary. The melt induces a discontinuous increase in the rate of atomic diffusion, which possibly favours growth of some surfaces of the grains at the expense of others. A similar technique was used previously to determine the solidus of basalt in a laser-heated diamond anvil cell[19].

Some experimental charges were quenched at temperatures just below or just above the onset of melting to probe the textural evolution using a scanning electron microscope (SEM). Under subsolidus conditions, the starting material appears well recrystallized into grains of several microns with polygonal shape (Fig. 2). A good textural equilibrium is evidenced by sharp grain-boundary angles, often close to 120°, and linear grain boundaries in between junctions[20]. Based on chemical maps, the mineralogical content at 5 GPa, for example, is an intimate mixture of olivine, clinopyroxene, orthopyroxene and garnet. No remaining traces of the glass starting material were observed. Above the solidus, we could observe some melt after an extensive search using the SEM. The melt occurs in the shape of very thin films along grain boundaries and nanometre-size pockets at triple junctions, as typically observed in partially molten systems[21,22]. Due to the short duration of the experiments, the microstructure may not correspond to full equilibrium. However, one can estimate the degree of partial melting to less than 1%, based on the fraction of sample surface covered by the melt (the most-shiny regions). The melt composition could not be determined accurately because of chemical interferences with the composition of surrounding minerals.

Based on the new mantle solidus and using $T_0 = 1{,}373$ K at room pressure[23], we calculated an equation of melting using the Simon and Glatzel (SG)[24] equation $[T_m(P) = T_0(P/a+1)^{1/c}]$. In this equation, a and c are adjustable parameters and P is pressure (Supplementary Table 3). A similar SG equation can model the dry liquidus reported in previous studies performed on KLB-1 peridotite[8,25]. The change in chemical composition, for example, between KLB peridotite and the chondritic-type mantle used in this study could induce significant differences in the solidus and liquidus temperatures[23]. However, the data set on the melting properties of the mantle-relevant compositions at mantle depths higher than 100–150 km remains insufficient to discuss these potential differences, which are therefore included in the uncertainties.

Comparison with previous melting studies

Although our data set is consistent with previous studies below 3–4 GPa (our study is not more precise than previous works at low pressures), it shows a mantle solidus lower than those previously reported for higher pressures (Fig. 3). The difference is, on average, 250 K for mantle depths greater than 200 km. The only study in close agreement with ours is that performed on an Allende-meteorite type composition, which included sulfur in the starting material[11]. The reason for the discrepancy with other studies can be manifold:

(1) Some previous studies used compositions that were too simplistic to represent properly the mantle state, for example, the CMAS composition used in Litasov and Ohtani[12]. For such a composition, the onset of melting may only occur when the pseudo-eutectic temperature is reached. In our study, the starting material contains Fe, Ti, Cr and Na in addition to the

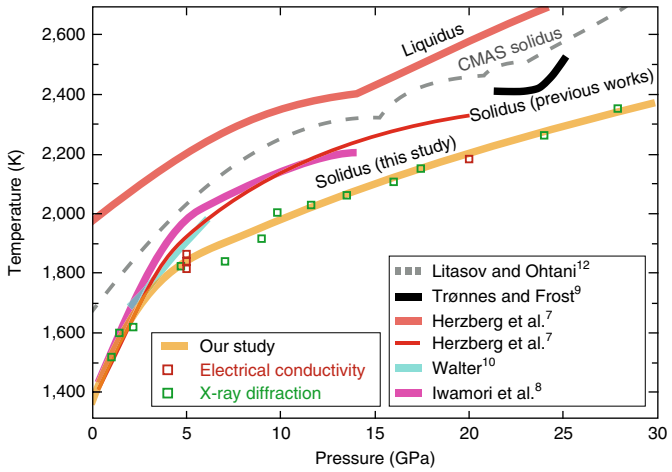

Fig. 3 | The new solidus temperature profile. The onset of the melting of a chondritic-type mantle composition was determined up to 28 GPa using EC (red squares) and X-ray diffraction (green squares). The new solidus is compared with previous studies performed using the quench method on the peridotitic mantle[7–10] or the simplified CMAS[12] composition. The new solidus plots significantly lower at pressures above 4–5 GPa.

CMAS basis. It was shown that such compositional changes can yield a difference of solidus temperature of a couple 100 K (refs [7,23]).

(2) The major melting criterion used in previous studies is the observation of molten regions in recovered samples. The formation of melt pockets can be difficult to detect at the lowest F values. Previous studies dedicated to this matter have established special techniques to detect the onset of melting[14,26]. However, the SEM images published in previous works correspond to an extremely high F, with a large fraction of the sample fully molten[9,12,25]. In contrast, our two in situ techniques are very sensitive to detect the onset of melting (Methods). In a previous study, the transmission electron microscope was used to differentiate grains that were solid at high temperature from secondary grains that rapidly recrystallized at the grain interfaces on quenching[7]. Some of the reported experiments show the absence of melt at temperatures higher than our new solidus temperatures, which we can only try to explain by the next point.

(3) Previous studies used mixtures of oxide powders with typical grain sizes on the order of micrometres. The heterogeneous grain composition does not favour the occurrence of nanoscale regions with the chemical composition of the solidus melt. Significant atomic diffusion is needed, over a distance typical of the grain size, to induce melting at the solidus temperature. The mean atomic path is estimated to be less than 10 nm per minute in the solid state at 2,000 K (ref. [27]). Therefore, kinetic effects, which were not taken into account in previous studies, can largely inhibit the melting of a mixture of oxides at the solidus temperature. In contrast, we used a glass with an ideal chemical homogeneity at the atomic scale. Chemical interactions are much facilitated, even though the glass eventually recrystallized in nanograins above the glass–liquid transition temperature, as observed in our study.

Only a few studies report the value of F at temperatures between the solidus and the liquidus at upper mantle conditions and these studies do not agree well with each other (Supplementary Fig. 9). The disagreement could come from differences in the chemical composition between the starting materials (peridotite[8], garnet–peridotite[10] or CMAS[12]) or to a difficult control of P–T conditions during the melting experiments. A theoretical study dedicated to the melting behaviour at relatively low pressure shows that the melt productivity can be highly variable with pressure, temperature and chemical composition[28]. In particular, the nature and the concentration of incompatible elements (Na and K) and *a fortiori* of volatile elements (H, C and S) can help to maintain relatively low F values over a significant temperature range above the solidus. Therefore, although the two in situ techniques used in this study are well suited to determine the solidus (because they can detect a small amount of melt), the variation of F with temperature between the solidus and the liquidus remains uncertain. This matter requires additional experimental studies.

Partial melting in the mantle today

We now compare our solidus profile with geotherms reported for the first 700 km mantle depths (Supplementary Fig. 1). First, we remember that the shallow temperature profile depends on the type of geological setting: the younger is the crust, the steeper is the thermal gradient close to the Earth's surface. Nevertheless, all the geotherms meet a mean adiabatic temperature gradient at mantle depths greater than ~250 km (ref. [13]). At the present-day, the surface potential temperature (T_p) is reported from ~1,600 K to a maximum of 1,750 K (ref. [29]). Both oceanic and continental lithosphere geotherms[30] currently plot at lower temperatures than the solidus, in agreement with a mantle state that is essentially solid. In that sense, our new measurements confirm that the possible occurrence of partial melting in specific regions of the upper mantle, suggested by geophysical measurements[3,22], should be dominated by the role of volatiles (H_2O and CO_2). Still, the lower solidus temperature makes upper-mantle partial melting easier than previously thought.

Partial melting in the Archaean mantle

Studies of non-arc basalts of Archaean and Proterozoic ages have revealed that the mantle T_p was significantly higher, by 50–100 K or more, compared with the present-day maximum T_p of ~1,750 K (refs [31–33]). Komatiitic lavas, which are generated from hotter mantle plumes, also point to a significantly hotter mantle temperature in the past. The shallow temperature profile was also different during the Archaean. The internal heat production was twice to four times that of today[34], which favours a steeper temperature profile in the lithosphere. Other effects instead favour a thicker lithosphere: (1) the early Earth initially operated in a regime dominated by a stagnant lid, with only episodic subduction of ageing plates[35] and (2) the transport of heat to the surface could have been dominated by intense volcanism, which plays a heat-pipe role[36]. Altogether, it was modelled that the early temperature profile in the shallow mantle could have lain in between the steeper oceanic and milder continental profiles[37] (Fig. 4 and Supplementary Fig. 1).

According to our results, an increase in the T_p of the ambient mantle above 1,800–1,850 K should generate a partially molten layer within the upper mantle (Fig. 4). Comparable slopes between the mantle solidus and the adiabatic gradient at depths greater than 200–250 km make $T_p \approx 1{,}900$ K a maximum value before intensive melting occurs in the entire upper mantle. It is actually possible that the value of $T_p = 1{,}900$ K was reached just after crystallization of the early magma ocean; a higher T_p would be associated with high F values, which implies a low viscosity that favours a rapid mantle cooling[38]. Our discussion does not include the role of volatile elements (H_2O and CO_2), because their concentrations in the early mantle remain poorly constrained. Their presence is expected to decrease the mantle solidus and favour mantle melting, possibly at T_p values significantly lower than 1,900 K. A partially molten layer could remain stable for long geological ages, because melts can be neutrally buoyant at mantle depths within a couple of hundred kilometres above the 410 km mantle discontinuity[39,40].

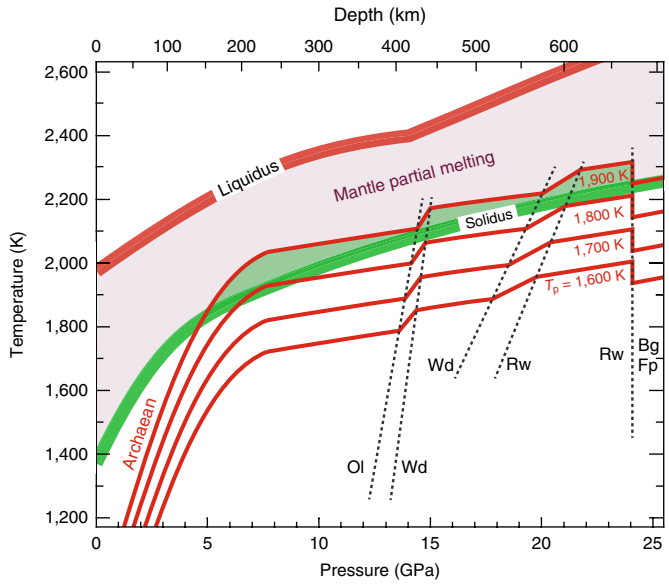

Fig. 4 | Partial melting in the early mantle. The current adiabatic profile of the mantle corresponds to a surface T_p between 1,600 K and up to 1,750 K (Supplementary Fig. 1). At the Archaean-to-Proterozoic transition, T_p was significantly higher, at 1,800–1,850 K (ref. [31]). For a T_p even higher than 1,800–1,850 K, a large part of the upper mantle should be partially molten. The transition between the younger, relatively hot and largely molten mantle and the older, colder and less molten mantle could have played a major role in the change of mantle dynamics at the transition. Ol, olivine; Wd, wadsleyite; Rw, ringwoodite; Bg, bridgmanite; Fp, ferropericlase.

Mantle changes at the Archaean-to-Proterozoic transition

The Archaean-to-Proterozoic transition is associated with major changes in the mantle dynamics with a progressive establishment of modern plate tectonics[32,35]. An increasing number of arc signatures in greenstone belts younger than 3.5 Ga suggests that slab subduction became a more-common process after this transition. This global change could be correlated to a transition in the upper-mantle mechanical properties. Indeed, it was shown that the coupling strength between tectonic plates and the underlying mantle is inversely proportional to the viscosity at the lithosphere–asthenosphere interface[41–43]. A hotter mantle during the Archaean would favour the formation of a partially molten layer and the mechanical weakening at a mid-upper-mantle depth. In addition, shear deformation can produce laminated lithologies and aligned melt accumulations, with further weakening[44]. Therefore, the presence of a partially molten layer could have favoured the early geodynamic regime dominated by a stagnant lid.

With secular mantle cooling, the degree of partial melting in the upper mantle eventually decreased. At one point, the state of the upper mantle became comparable to the present-day situation, in which partial melting still takes place, but at relatively low F values[22]. The decrease of F below a certain threshold value should be associated with a mechanical hardening, which favours mechanical coupling at the lithosphere–asthenosphere interface. This transition could have induced the change of geodynamic regime at the Archaean-to-Proterozoic transition.

Methods

Methods, including statements of data availability and any associated accession codes and references, are available at https://doi.org/10.1038/s41561-017-0053-9.

Received: 26 June 2017; Accepted: 13 December 2017;
Published online: 22 January 2018

References

1. Solomatov, V. S. in *Treatise on Geophysics* Vol. 9 (ed. G. Schubert) 81–104 (Elsevier, Amsterdam, 2015).
2. Romanowicz, B. A global tomographic model of the shear attenuation in the upper mantle. *J. Geophys. Res. Solid Earth* **100**, 12375–12394 (1995).
3. Tauzin, B., Debayle, E. & Wittlinger, G. Seismic evidence for a global low-velocity layer within the Earth's upper mantle. *Nat. Geosci.* **3**, 718–721 (2010).
4. Lay, T., Garnero, E. J. & Williams, Q. Partial melting in a thermo-chemical boundary layer at the base of the mantle. *Phys. Earth Planet. Inter.* **146**, 441–467 (2004).
5. Ferot, A. & Bolfan-Casanova, N. Water storage capacity in olivine and pyroxene to 14 GPa: implications for the water content of the Earth's upper mantle and nature of seismic discontinuities. *Earth Planet. Sci. Lett.* **349**, 218–230 (2012).
6. Aubaud, C., Hauri, E. H. & Hirschmann, M. M. Hydrogen partition coefficients between nominally anhydrous minerals and basaltic melts. *Geophys. Res. Lett.* **31**, L20611 (2004).
7. Herzberg, C., Raterron, P. & Zhang, J. New experimental observations on the anhydrous solidus for peridotite KLB-1. *Geochem. Geophys. Geosyst.* **1**, 1051 (2000).
8. Iwamori, H., McKenzie, D. & Takahashi, E. Melt generation by isentropic mantle upwelling. *Earth Planet. Sci. Lett.* **134**, 253–266 (1995).
9. Trønnes, R. G. & Frost, D. J. Peridotite melting and mineral–melt partitioning of major and minor elements at 22–24.5 GPa. *Earth Planet. Sci. Lett.* **197**, 117–131 (2002).
10. Walter, M. J. Melting of garnet peridotite and the origin of komatiite and depleted lithosphere. *J. Petrol.* **39**, 29–60 (1998).
11. Agee, C. B., Li, J., Shannon, M. C. & Circone, S. Pressure–temperature phase-diagram for the Allende meteorite. *J. Geophys. Res. Solid Earth* **100**, 17725–17740 (1995).
12. Litasov, K. & Ohtani, E. Phase relations and melt compositions in CMAS–pyrolite–H_2O system up to 25 GPa. *Phys. Earth Planet. Inter.* **134**, 105–127 (2002).
13. Katsura, T., Yoneda, A., Yamazaki, D., Yoshino, T. & Ito, E. Adiabatic temperature profile in the mantle. *Phys. Earth Planet. Inter.* **183**, 212–218 (2010).
14. Laporte, D., Toplis, M. J., Seyler, M. & Devidal, J. L. A new experimental technique for extracting liquids from peridotite at very low degrees of melting: application to partial melting of depleted peridotite. *Contrib. Mineral. Petrol.* **146**, 463–484 (2004).
15. Sifre, D. et al. Electrical conductivity during incipient melting in the oceanic low-velocity zone. *Nature* **509**, 81–85 (2014).
16. Sato, H. & Ida, Y. Low frequency electrical impedance of partially molten gabbro: the effect of melt geometry on electrical properties. *Tectonophysics* **107**, 105–134 (1984).
17. Partzsch, G. M., Schilling, F. R. & Arndt, J. The influence of partial melting on the electrical behavior of crustal rocks: laboratory examinations, model calculations and geological interpretations. *Tectonophysics* **317**, 189–203 (2000).
18. Maumus, J., Bagdassarov, N. & Schmeling, H. Electrical conductivity and partial melting of mafic rocks under pressure. *Geochim. Cosmochim. Acta* **69**, 4703–4718 (2005).
19. Andrault, D. et al. Melting of subducted basalt at the core–mantle boundary. *Science* **344**, 892–895 (2014).
20. Davis, F. A., Hirschmann, M. M. & Humayun, M. The composition of the incipient partial melt of garnet peridotite at 3 GPa and the origin of OIB. *Earth Planet. Sci. Lett.* **308**, 380–390 (2011).
21. Yoshino, T., Laumonier, M., McIsaac, E. & Katsura, T. Electrical conductivity of basaltic and carbonatite melt-bearing peridotites at high pressures: implications for melt distribution and melt fraction in the upper mantle. *Earth Planet. Sci. Lett.* **295**, 593–602 (2010).
22. Chantel, J. et al. Experimental evidence supports mantle partial melting in the asthenosphere. *Sci. Adv.* **2**, e1600246 (2016).
23. Hirschmann, M. M. Mantle solidus: experimental constraints and the effects of peridotite composition. *Geochem. Geophys. Geosyst.* **1**, C000070 (2000).
24. Simon, F. & Glatzel, G. Fusion–pressure curve. *Z. Anorg. Allg. Chem.* **178**, 309–316 (1929).
25. Zhang, J. & Herzberg, C. Melting experiments on anhydrous peridotite KLB-1 from 5.0 to 22.5 GPa. *J. Geophys. Res.* **99**, 17729–17742 (1994).
26. Hirose, K. & Kushiro, I. Partial melting of dry peridotite at high-pressures—determination of compositions of melts segregated from peridotite using aggregates of diamonds. *Earth Planet. Sci. Lett.* **114**, 477–489 (1993).

27. Béjina, F., Jaoul, O. & Liebermann, R. C. Diffusion in minerals at high pressure: a review. *Phys. Earth Planet. Inter.* **139**, 3–20 (2003).
28. Hirschmann, M. M., Asimow, P. D., Ghiorso, M. S. & Stolper, E. M. Calculation of peridotite partial melting from thermodynamic models of minerals and melts. III. Controls on isobaric melt production and the effect of water on melt production. *J. Petrol.* **40**, 831–851 (1999).
29. Dalton, C. A., Langmuir, C. H. & Gale, A. Geophysical and geochemical evidence for deep temperature variations beneath mid-ocean ridges. *Science* **344**, 80–83 (2014).
30. Litasov, K. D., Shatskiy, A. & Ohtani, E. Melting and subsolidus phase relations in peridotite and eclogite systems with reduced C–O–H fluid at 3–16 GPa. *Earth Planet. Sci. Lett.* **391**, 87–99 (2014).
31. Herzberg, C., Condie, K. & Korenaga, J. Thermal history of the Earth and its petrological expression. *Earth Planet. Sci. Lett.* **292**, 79–88 (2010).
32. Kamber, B. S. The evolving nature of terrestrial crust from the Hadean, through the Archaean, into the Proterozoic. *Precambrian Res.* **258**, 48–82 (2015).
33. Arndt, J., Barnes, S. J. & Lesher, C. M. *Komatiite* (Cambridge Univ. Press, Cambridge, 2008).
34. Korenaga, J. Initiation and evolution of plate tectonics on Earth: theories and observations. *Annu. Rev. Earth Planet. Sci.* **41**, 117–151 (2013).
35. van Hunen, J. & Moyen, J.-F. in *Annual Review of Earth and Planetary Sciences* Vol. 40 (ed. R. Jeanloz) 195–219 (Annual Reviews, Palo Alto, CA, 2012).
36. Moore, W. B. & Webb, A. A. G. Heat-pipe Earth. *Nature* **501**, 501–505 (2013).
37. Michaut, C. & Jaupart, C. Secular cooling and thermal structure of continental lithosphere. *Earth Planet. Sci. Lett.* **257**, 83–96 (2007).
38. Monteux, J., Andrault, D. & Samuel, H. On the cooling of a deep terrestrial magma ocean. *Earth Planet. Sci. Lett.* **448**, 140–149 (2016).
39. Matsukage, K. N., Jing, Z. C. & Karato, S. Density of hydrous silicate melt at the conditions of Earth's deep upper mantle. *Nature* **438**, 488–491 (2005).
40. Sakamaki, T., Suzuki, A. & Ohtani, E. Stability of hydrous melt at the base of the Earth's upper mantle. *Nature* **439**, 192–194 (2006).
41. Sizova, E., Gerya, T., Brown, M. & Perchuk, L. L. Subduction styles in the Precambrian: insight from numerical experiments. *Lithos* **116**, 209–229 (2010).
42. Foley, B. J., Bercovici, D. & Elkins-Tanton, L. T. Initiation of plate tectonics from post-magma ocean thermochemical convection. *J. Geophys. Res. Solid Earth* **119**, 8538–8561 (2014).
43. Doglioni, C., Ismail-Zadeh, A., Panza, G. & Riguzzi, F. Lithosphere–asthenosphere viscosity contrast and decoupling. *Phys. Earth Planet. Inter.* **189**, 1–8 (2011).
44. Jin, Z. M., Green, H. W. & Zhou, Y. Melt topology in partially molten mantle peridotite during ductile deformation. *Nature* **372**, 164–167 (1994).

Acknowledgements

We thank A. Bouhifd, N. Cayzer, M. Guitreau, T. Kawamoto, T. Komabayashi, D. Laporte, M. Laumonier, H. Martin, S. Parman, B. Reynard and F. Schiavi for help and fruitful discussions. This work was supported by the French National Research Agency (ANR) contract 'OxyDeep'. This research was financed by the French Government Laboratory of Excellence initiative no. ANR-10-LABX-0006, the Région Auvergne and the European Regional Development Fund. This is Laboratory of Excellence ClerVolc contribution number 279.

Author Contributions

L.H. and G.P. synthesized the glass starting material. G.P. and G.M. performed the EC measurements. G.P., D.A., G.M., N.B.C., D.N., N.G. and A.K. performed the X-ray diffraction measurements, which were subsequently treated by D.A. G.P. and N.B.C. determined the water content in samples using infrared spectroscopy. D.A. wrote the manuscript with help from G.P., G.M. and J.M. All of the authors discussed and commented on various versions of the manuscript.

Additional information

Supplementary information is available for this paper at https://doi.org/10.1038/s41561-017-0053-9.

Reprints and permissions information is available at www.nature.com/reprints.

Correspondence and requests for materials should be addressed to D.A.

Publisher's note: Springer Nature remains neutral with regard to jurisdictional claims in published maps and institutional affiliations.

Methods

Preparation of starting material. Our sample consisted of a mixture of oxides with the composition of the chondritic mantle after core segregation (Supplementary Table 1). We selected this composition because it could represent well both the early Earth's mantle and the deep mantle today. Our composition includes the minor elements Ti, Cr and Na, in addition to the major Si, Mg, Al, Fe and Ca elements. This is an important difference with some previous works based on simplified composition (for example, the CMAS composition[12]). No trace elements were added, as their effect on the solidus is negligible as long as their solubility limit in solid phases is not exceeded[45].

Under upper-mantle *P*–*T* conditions, we expect the sample mineralogy dominated, on the one hand, by olivine and its high-pressure polymorphs (wadsleyite (Wd) and ringwoodite (Rw)) and, on the other hand, a variable amount of pyroxenes and majoritic garnet. In our experiments, these lithologies were confirmed by in situ X-ray diffraction (see below). Final-phase fractions may be slightly different than those present in the mantle, first because the true mantle composition remains relatively open and second because of potential chemical heterogeneities. The chemical activities of the major and minor elements should not be largely different if the model composition changes between peridotite, pyrolite or chondritic-type materials. Therefore, these compositions should present similar solidus temperatures.

The mixture of oxides was ground in an agate mortar for approximately 1 h to ensure a homogeneous powder. Then, glass spheres of ~2.5 mm in diameter were prepared using the high-temperature aerodynamic levitation technique associated with CO_2 laser heating at CNRS[46]. This containerless method uses a conical nozzle that enables the diffusion of a regulated gas flow below the sample, which eliminates completely any contact between the sample and the container. In this process, the powder is first cold-pressed under a load of 6 tons. Weighted pieces of the recovered agglomerate are then melted at a temperature above 2,273 K, which gives a spherical shape to the sample. After a couple of minutes, samples were quenched to room temperature with a typical cooling rate of 500 K s^{-1}. The gas used for the sample levitation was pure Ar, with less than 0.05 ppm of oxygen; however, the vessel remained open to air during the synthesis at high temperature. This prevents the formation of metallic Fe at very high temperatures when using a reduced atmosphere.

For each experiment, an initial sphere of glass 2–3 mm in diameter was reshaped in the form of a cylinder and directly inserted into the capsule of the high-pressure assembly. Such a starting material provides consistent advantages when performing studies of the melting behaviour. First, the amount of moisture adsorbed at the sample surface is drastically reduced compared with that adsorbed by a powder (Supplementary Fig. 2). Second, the glass presents an ideal chemical homogeneity (as confirmed by electron microprobe analyses) compared with the intrinsic heterogeneities typical of mixtures of oxide powders.

Determination of the water content in our samples. Infrared spectroscopy was performed to determine the H_2O content in our samples before and after the melting experiment. Infrared spectra were measured in air on double-polished sections with thicknesses of 600 µm (for the glass starting material) or 900 µm (for the recovered samples). Spectra were collected between 700 and 7,000 cm^{-1} with 2 cm^{-1} steps and 300 scans for the sample and 100 scans for the background. In the starting glass, we measured less than 1 ppm wt H_2O, which indicates a starting material nominally dry. For samples recovered from high-pressure–high-temperature conditions, the grain size was significantly smaller (Fig. 2) than the infrared beam. We performed several measurements within the same sample, which appeared to be consistent with each other. From the broad asymmetric band centred at 3,500 cm^{-1} and the OH peaks related to point defects in olivine[5] at 3,572, 3,527 and 3,357 cm^{-1}, we calculate a H_2O content of ~90 ppm (Supplementary Fig. 2). These observations confirm that the H_2O contamination remained very limited during the melting experiments. The sample H_2O content on melting is critical because the presence of volatile elements can induce a significant decrease in the melting temperature. Still, due to the presence of 90 ppm water in our samples, we corrected all experimental solidus temperatures by +35 to +55 K, based on the previously reported cryoscopic relation[47] (Supplementary Table 2).

EC measurements. We measured the EC of our samples up to their melting point in a 1,500-ton 6-8 split cylinder Kawai-type multi-anvil apparatus at the Laboratory of Magmas and Volcanoes in Clermont-Ferrand. Quasi-hydrostatic pressures of 5 or 20 GPa were obtained using eight tungsten–carbide cubic anvils with edges truncated to 11 or 4 mm, respectively (Supplementary Figs. 3 and 4). We used an octahedral pressure medium with an edge length of 18 or 10 mm made of semisintered MgO with 5% Cr_2O_3. The pressure calibration for these assemblages has an uncertainty of ~0.5 GPa (ref. [48]). The heater was made of a 50 µm thick Re foil folded into a cylindrical shape and inserted in the ZrO_2 sleeve, which served as a thermal insulator. We applied an alternating current with a frequency of 100 Hz to generate temperatures up to more than 2,500 K. A cylindrical sleeve of MgO was inserted between the heater and the sample to prevent chemical reactions with the Re heater, ensure electrical insulation of the sample and maintain the sample shape on melting.

Temperatures were measured using type C thermocouple ($WRe_{5\%}$–$WRe_{26\%}$). We added a third $WRe_{5\%}$ wire to the opposite side of the cylindrical sample to allow measurements of the sample impedance. Two Re discs were placed on the top and bottom of the cylindrical sample. The discs served as electrodes for EC measurements. As the determination of temperature gradients is essential in this work, we modelled thermal gradients in the cell assembly based on a finite-element method[49] for thermocouple temperatures between 1,473 and 2,273 K (Supplementary Fig. 3b). As expected, the hottest part is found at the centre of the sample (extreme top-left position in Supplementary Fig. 3b). Each temperature contour (thin black lines) represents a temperature interval of 50 K in Supplementary Fig. 3b. In all the simulations, the temperature difference (ΔT_{Simul}) between the sample centre and the thermocouple does not exceed 100 K. We therefore apply a temperature correction of ΔT_{Simul} to all our temperature measurements (Supplementary Table 2).

The sample EC was determined using the impedance spectroscopy method in the frequency range of 10^6 to 10^1 Hz (ref. [50]) (Supplementary Fig. 4). The insulation resistance (detection limit) of the assembly was determined at similar pressure–temperature conditions prior to the actual experiments. Polycrystalline samples are characterized by a combination of resister and constant-phase element (R-C/CPE) circuits and the resistance can be obtained by fitting the impedance spectra to appropriate equivalent circuits. Once the sample resistance has been determined, conductivity can be calculated using the sample diameter and length measured after each experiment, assuming the sample geometry remains unchanged during the experiment. The activation enthalpy (ΔH) of each conduction mechanism can be obtained by fitting data to the Arrhenius equation, where σ is the EC (S m^{-1}), T is the absolute temperature, σ_0 is the pre-exponential factor (S m^{-1}) and k is the Boltzmann constant (J K^{-1}):

$$\sigma = \sigma_0 \, e^{(-\Delta H/kT)}$$

For each experiment, we performed a series of heating and cooling cycles, similar to those in previous works[51] (Supplementary Fig. 5a). In a first heating cycle, below 573 K, a low activation enthalpy is likely to result from an extrinsic mechanism associated with the presence of free protons (adsorbed moisture, mostly around the sample). At the desired pressure, a sample was kept at 573 K for more than 12 h. While maintaining 573 K, the electrical resistance of the sample was measured along regular intervals and the next heating cycle started once the sample resistance reached a steady value, which is often 1–2 orders of magnitude higher than the resistance measured at the beginning of the heating cycle. This crucial step ensures the removal of the absorbed moisture from the sample and the surrounding assembly materials. The absorbed moisture could otherwise interfere with measurements at higher temperatures.

The crystallization of our samples was observed between 1,370 and 1,570 K, thus at temperatures at least 300 K below the solidus temperature (Supplementary Table 2). The temperature was kept constant above the crystallization temperature for 2–3 h to allow full crystallization of the initial glass samples. The EC of the crystalline samples was measured in several heating and cooling cycles until the heating and cooling paths were reproducible.

The crystallized samples show an activation energy of 1.02 eV (Fig. 1, green line). This is typical of a conduction mechanism with electron hole hopping between Fe^{2+} and Fe^{3+} (small polaron conduction)[50]. At a temperature of ~1,700 K for a nominal pressure of 5 GPa, we observe a first-order change of slope in the conductivity profile (Fig. 1, blue line). The change of slope can be interpreted as the first occurrence of an interconnected partial melt. The experimental uncertainty for the determination of the solidus temperature is about ±25 degree. The errors associated with EC measurements were less than 5%, and were mainly associated with temperature estimations, data-fitting errors and the estimation of sample dimensions. A good reproducibility is observed for EC profiles obtained for our different samples (Supplementary Fig. 5b). Our EC results compare well with ECs of both solid minerals and melts reported in previous studies.

X-ray diffraction measurements. In situ X-ray diffraction experiments were performed using the 1,200-ton DIA-type multi-anvil apparatus installed at the PSICHE beamline of the SOLEIL synchrotron in Gif-sur-Yvette. Pressures up to 28 GPa (Supplementary Table 2) were generated using a 7/3 multi-anvil assembly configuration. We used 14 mm WC cubes as secondary anvils (Supplementary Fig. 6). Similar to EC measurements, we used semisintered MgO with a 5% Cr_2O_3 octahedron pressure media and a cylindrical ZrO_2 sleeve in which a 50 µm thick Re-foil heater was inserted. The cylindrical sample of chondritic glass was inserted into an MgO capsule. The Re furnace was oriented horizontally to allow an X-ray beam path parallel to the Re tube. To apply electrical power, two Re electrodes were placed in contact with the furnace. Temperature was measured using a W/Re thermocouple that touched the Re furnace. The thermocouple signal was filtered to remove the common electrical mode at 100 Hz. We used alternatively gaskets made of pyrophilite or a mixture of boron and epoxy. The sample pressure was determined based on the pressure–volume–temperature equation of state of MgO of its capsule, with an accuracy of ~0.5 GPa.

At PSICHE, an under-vacuum wiggler produces a white X-ray beam with energy range from 20 to more than 80 keV. The X-ray beam is focused vertically

between the anvil gap of the multi-anvil apparatus using a horizontal mirror located at 18.5 m from the source and 4 m from the sample. The resulting vertical full-width at half-maximum of the beam at the sample position is approximately 20 µm, which corresponds to almost a one order of magnitude flux gain compared with the unfocused beam. The beam is then collimated horizontally to a typical width of 50 µm. Two different modes were used: (1) samples were first aligned in the beam using X-ray radiography, for which the press was scanned vertically in the X-ray beam and the image was then reconstructed numerically (Supplementary Fig. 6c), and (2) diffraction was performed in an energy-dispersive mode using a Caesar-type diffractometer[52]. A best resolution in interplanar distance d_{hkl} is achieved when the diffracted X-ray beam is collimated horizontally to ~50 µm by two slit systems located after the sample. A typical diffraction 2θ angle of 8.0° is convenient to register the major diffraction lines of our silicate samples. The resolution in diffraction angle is about 10^{-3} degrees.

On heating, the sample temperature was kept at 700 K for several minutes to remove the adsorbed moisture in the transmitting media. This procedure also mimics the experimental procedure followed for EC measurements. We then increased the temperature until sample crystallization was observed, based on a clear evolution of X-ray diffraction (Supplementary Table 2). At this point, we wait several minutes to finalize the grain growth until no significant change with time was observed on the diffraction pattern. At temperatures below the solidus, the absence of melt prevents the atomic diffusion required for additional grain growth in such a multiphasic system (that is, the Ostwald ripening effect[53] (Fig. 3)).

For each phase, relative intensities between different diffraction peaks follow quite well those theoretically expected based on the atomic packing in the unit-cell lattice (Supplementary Fig. 6). Such an achievement is typical of very small grains in a sample free of stresses. Still, the use of the energy-dispersive X-ray diffraction technique (compared with the angle-dispersive one) prevents the refinement of phase fractions for the coexisting olivine (or its high-pressure polymorphs), garnet and pyroxenes phases present in our samples. In addition, the limited energy resolution of the Ge detector produces peaks that overlap and the identification of minor phases sometimes becomes difficult. In contrast, this method enables the acquisition of a decent X-ray-diffraction pattern every few seconds, which offers new criteria for the determination of the solidus temperature.

Analysis of recovered samples. Recovered samples were cut in two using a diamond-wire saw. A sample half was embedded in epoxy, polished to a mirror-like surface and coated with a thin layer of carbon using a low-vacuum sputter-coater machine. Textural and semiquantitative chemical analyses were performed using a JEOL JSM-5910 LV SEM equipped with a PGT microanalysis system at Laboratory of Magmas and Volcanoes and a Carl Zeiss SIGMA HD VP Field Emission SEM with an Oxford AZtec ED X-ray analysis operated at the University of Edinburgh. Textural analyses with a field-emission gun SEM were performed at a high accelerating voltage (15 kV) and a small working distance (6–10 mm). These conditions are ideal to detect small features in samples with a low degree of partial melting. For the semiquantitative analysis based on X-ray fluorescence, we instead used a working distance of 20 mm. Energy was also lowered to 5 kV to minimize the penetration of electrons in samples and, consequently, to optimize the spatial resolution.

Data availability. The data that support the findings of this study are available from the corresponding author on request.

References

45. Corgne, A., Liebske, C., Wood, B. J., Rubie, D. C. & Frost, D. J. Silicate perovskite-melt partitioning of trace elements and geochemical signature of a deep perovskitic reservoir. *Geochim. Cosmochim. Acta* **69**, 485–496 (2005).
46. Hennet, L. et al. Aerodynamic levitation and laser heating: applications at synchrotron and neutron sources. *Eur. Phys. J. Spec. Top.* **196**, 151–165 (2011).
47. Tenner, T. J. & Hirschmann, M. M. & Humayun, M. The effect of H_2O on partial melting of garnet peridotite at 3.5 GPa.*Geochem. Geophys. Geosyst.* **13**, Q03016 (2012).
48. Boujibar, A. et al. Metal–silicate partitioning of sulphur, new experimental and thermodynamic constraints on planetary accretion. *Earth Planet. Sci. Lett.* **391**, 42–54 (2014).
49. Hernlund, J., Leinenweber, K., Locke, D. & Tyburczy, J. A. A numerical model for steady-state temperature distributions in solid-medium high-pressure cell assemblies. *Am. Miner.* **91**, 295–305 (2006).
50. Yoshino, T. Laboratory electrical conductivity measurement of mantle minerals. *Surv. Geophys.* **31**, 163–206 (2010).
51. Manthilake, M. et al. Electrical conductivity of wadsleyite as a function of temperature and water content. *Phys. Earth Planet. Inter* **174**, 10–18 (2009).
52. Wang, Y. B. et al. A new technique for angle-dispersive powder diffraction using an energy-dispersive setup and synchrotron radiation. *J. Appl. Crystallogr.* **37**, 947–956 (2004).
53. Yamazaki, D., Kato, T., Ohtani, E. & Toriumi, M. Grain growth rates of $MgSiO_3$ perovskite and periclase under lower mantle conditions. *Science* **274**, 2052–2054 (1996).